AGU PUBLICATIONS

JGR

Journal of Geophysical Research: Space Physics



RESEARCH ARTICLE
10.1002/2016JA022997

**Key Points:**
- Over 4 year comparison of FPI and meteor radar wind over China
- Correlation coefficient of FPI/MR wind stronger for meridional than zonal stronger at 87 km than 97 km
- Influence of airglow variation on FPI wind

**Correspondence to:**
T. Yu,
yutaommnn@163.com

**Citation:**
Yu, T., C. Xia, X. Zuo, C. Huang, T. Mao, L. Liu, and Z. Liu (2016), A comparison of mesospheric and low-thermospheric winds measured by Fabry-Perot interferometer and meteor radar over central China, *J. Geophys. Res. Space Physics*, *121*, 10,037–10,051, doi:10.1002/2016JA022997.

Received 27 MAY 2016
Accepted 31 AUG 2016
Accepted article online 2 SEP 2016
Published online 1 OCT 2016



# A comparison of mesospheric and low-thermospheric winds measured by Fabry-Perot interferometer and meteor radar over central China

**Tao Yu[1,2], Chunliang Xia[1], Xiaomin Zuo[1], Cong Huang[3], Tian Mao[2], Libo Liu[4], and Zhizhao Liu[2]**

[1]Hubei Subsurface Multi-scale Imaging Key Laboratory, Institute of Geophysics and Geomatics, China University of Geosciences, Wuhan, China, [2]Department of Land Surveying and Geo-Informatics, The Hong Kong Polytechnic University, Hung Hom, Hong Kong, [3]Key Laboratory of Space Weather, National Center for Space Weather, China Meteorological Administration, Beijing, China, [4]Key Laboratory of Earth and Planetary Physics, Institute of Geology and Geophysics, Chinese Academy of Sciences, Beijing, China

**Abstract** Wind data observed by a Fabry-Perot interferometer (FPI) and a meteor radar (MR) deployed in two stations, which are 430 km apart in ground distance, are used to study wind climatology in mesosphere/lower thermosphere over central China and compare between the measurements. A general morphologic similarity of the FPI winds and MR winds is identified with 4 year data since November 2011. At 87 km, the wind vector plots show that the FPI and MR winds agree with each other very well in all months. The zonal winds of both instruments have an apparent semiannual variation with a maximal strength of −20 m/s at around 18:00 UT in equinoctial months, and the meridional winds from both instruments have an apparent annual variation with a maximal strength of −40 m/s at around 15:00 UT in summer months. The correlation coefficients between the measurements of the two instruments are about 0.95 for meridional wind and 0.90 for zonal wind. At 97 km, the wind vector plots show that FPI and MR winds agree with each other from May to October and are obviously different in the rest months. There are very weak semiannual variations at around 18:00 UT for both zonal winds and pronounced annual variation at around 13:00 UT for both meridional winds. The correlation coefficients between the FPI and MR winds are 0.73 for zonal wind and 0.86 for meridional wind, which are overall smaller than that at 87 km. A Gaussian distribution of airglow profile is used to investigate the deviations associated with peak height and full width at half maximum (FWHM) of airglow layer. It is found that the variation of peak height could lead to about 20% variation of correlation coefficients between measurements at the height of 87 km and about 14.8% at the height of 97 km on average. The variation of FWHM could lead to a correlation coefficient variation of about 2.4% and 3.5% at the height of 87 km and 97 km, respectively. Some other reasons, such as the influence of geomagnetic field on meteor trail and the propagation of gravity waves, could also contribute to these differences between measurements.

## 1. Introduction

The neutral winds play a very important role in dynamics in the upper atmosphere [*Fuller-Rowell*, 1995; *Fuller-Rowell et al.*, 2007]. However, the lack of neutral wind measurements hinders our dynamic studies in the upper atmosphere. Ground-based instruments such as incoherent scatter radar, meteor radar (MR), medium-frequency radar, lidar, Michelson interferometer, and Fabry-Perot interferometer (FPI) are all capable of detecting the wind and dynamics in the upper atmosphere [*Santos et al.*, 2011; *David et al.*, 2013; *Hocking*, 1997; *Phillips et al.*, 1994; *Yuan et al.*, 2006; *She et al.*, 2002; *Langille et al.*, 2013; *Wu et al.*, 2004]. Among them, the MR and FPI are two types of instruments to effectively detect waves and winds in the upper atmosphere at relatively low costs.

The MR, since it was first developed in 1949 [*Manning et al.*, 1950], has become a very useful instrument to observe winds in mesosphere/lower thermosphere (MLT). Currently, there are about one dozen of MR instruments operating all around the world, providing a large amount of MLT wind and temperature data. These data have been widely used to investigate the mean winds, tides, and planetary waves in the MLT. For instance, the first Japanese results reported the mean winds at 82–106 km altitude monitored by the Kyoto meteor radar (35°N, 136°E) over the period from May 1983 to December 1985, and the characteristics of semidiurnal tides and long-period wind oscillations have also been summarized [*Tsuda and Kato*, 1988; *Tsuda*

*et al*., 1988]. *Yamamoto et al*. [1986] studied the characteristics of gravity waves with periods longer than 2 h observed by the Kyoto meteor radar and found an apparent eastward phase velocity of a monochromatic gravity wave. The Australian new all-sky interferometric meteor radar system and new analysis techniques at Buckland Park, South Australia, were introduced by *Holdsworth et al*. [2004]. Wind measurements from a meteor radar in polar regions were described by *Forbes et al*. [1995] and *Fritts et al*. [2012]. A very good summary of radar instrumentation and techniques for studies of the upper atmosphere was given by *Hocking* [1997]. The first meteor radar in China region was deployed in 2003 [*Xiong et al*., 2004]. Zhao and others investigated features of tide and planetary wave observed by this MR [*Zhao et al*., 2005a, 2005b; *Jiang et al*., 2005; *Xiong et al*., 2006]. Recently, a meteor radar chain was established along the 120°E meridian in China, and observations of the horizontal wind in the MLT region from this radar chain were reported [*Yu et al*., 2013], and they found that the diurnal component dominated at the low-latitude stations while the semidiurnal component dominated at midlatitude stations.

The new FPI technology has great improvement in the sensitivity and observation resolution [*Ishii1 et al*., 1999; *Wu et al*., 2004] during the past decades. However, the global coverage of FPI observations is still very limited [*Meriwether*, 2006]. FPI-measured wind data are very valuable to the understanding of the dynamics and development of general circulation models in the thermosphere [*Rees et al*., 1984, 1990; *Fejer et al*., 2002; *Zhang et al*., 2003]. *Fejer et al*. [2002] studied the climatology of quiet time and storm time nocturnal winds with FPI measurements over Millstone Hill from 1989 to 1999. *Emmert et al*. [2003] focused on latitudinal gradient of quiet time thermospheric neutral wind over Millstone Hill. Later *Emmert et al*. [2006] studied the climatology of nighttime wind in the upper thermosphere during geomagnetic quiet conditions. *Wu et al*. [2005] showed strong day-to-day and interannual variations of the 12 h wave in the mesosphere winds by surveying multiyear data set from Resolute Bay station, Canada (75°N, 95°W). *Won et al*. [2007] studied tidal features of mesospheric temperature and neutral winds at that station. *Ammosov and Gavrilyeva* [2008] studied the temperature semidiurnal tide derived from nightglow observed at a Russia station (63°N, 129.5°E). A good review about the studies of thermospheric dynamics with FPI network was given by *Meriwether* [2006].

Comparisons between wind measurements by MR and FPI are helpful for the understanding of the dynamics process in MLT. FPI wind observations, which are weighted by the height profile of the airglow emission, are different from the MR wind data that have a good altitude resolution of 2–3 km. Thus, it is difficult to make a simple comparison between the two instruments. As early as in 1979, *Hernandez and Roper* [1979] compared wind measurements from a radio meteor over Atlanta (34°N, 84°W) with an airglow over Fritz Peak Observatory (39.8°N, 195.5°W). Although the two stations had a large separation, general agreements in both zonal and meridional wind vectors were found. *Lloyd et al*. [1990] compared the day-to-day variations of 1 month wind measurements from a medium-frequency radar and a FPI at Saskatoon (52°N, 107°W) and found that winds are generally similar between the two systems, with differences attributing to auroral contamination. *Phillips et al*. [1994] made a long-term comparison between a medium-frequency radar and a Fabry-Perot spectrometer with data from 1988 to 1992 and found that strong similarities could be found in both measurements in long-term time series, but apparent differences could be found in real-time data. *Plagmann et al*. [1998] compared simultaneous wind measurements from a Fabry-Perot spectrometer, a medium-frequency radar, and a meteor radar located at a New Zealand's South Island during the period of May 1997 to April 1998. Their results showed reasonable agreement among the three methods, in particular between the FPI and meteor radar. *Aruliah et al*. [2005] found direct evidence of mesoscale variability on ion-neutral dynamics using co-located FPI and European Incoherent Scatter radar. Many researchers also focused on making comparisons with model results. *Cervera and Reid* [2000] made a comparison of atmospheric parameters derived from meteor observations at Buckland Park with Committee on Space Research International Reference Atmosphere model. *Yuan et al*. [2013] and *Yu et al*. [2014] compared wind measurements by two newly built FPIs in China with the horizontal wind model.

In China, many new ground-based instruments include optical system and radars have been deployed in recent years. In 2010 and 2011, two FPIs were successfully deployed at Xinglong (40.2°N, 117.4°E) and Kelan (111.6°E, 38.7°N). *Yuan et al*. [2010, 2013] introduced the new observations of FPI system in Xinglong and studied the annual, semiannual, and terannual variations of the midnight winds observed by the FPI in Xinglong. *Jiang et al*. [2012] compared the simultaneous wind measurements from FPI and MR during April–May of 2010 and found that the variations of FPI winds were very consistent with meteor winds except

for some minor differences. *Yu et al*. [2014] and *Yao et al*. [2015] gave the results of thermospheric and mesospheric wind measurements observed over Kelan, China, respectively. Since there is lack of wind simultaneous measurements by FPI or MR at adjacent stations in China, comparison of wind measurements measured by the FPI and MR would be very helpful to investigate the winds and dynamics in the MLT over China, as well as make better use of respective instruments.

## 2. Data Selection and Analysis

The Kelan FPI (38.7°N, 111.6°E), which follows the same design of FPI at the Resolute Bay station, Canada [*Wu et al*., 2004], consists of the following components: dome, sky scanner, filter, etalon chamber (10 cm caliber with thermal control), mirror and lens focus mechanism, camera, and data acquisition and saving systems. A calibration technique by a frequency stabilized laser at 632.8 nm, a precise pressure- and temperature-controlled system, and a back-illuminated CCD detector with $1024 \times 1024$ pixels and $-50$°C operational temperature are used in this FPI system. This FPI had been calibrated and had a trial run for 1 month at the High Altitude Observatory (HAO), National Center for Atmospheric Research (NCAR), USA, before it was shipped to Kelan, China, for installation. A detailed schematic diagram can be found in *Wu et al*. [2004] and *Yuan et al*. [2010]. Controlled by a computer, the Kelan FPI operates in an automated mode on schedule. It is scheduled to shift the filter to observe at wavelengths of 892.0 nm, 630.0 nm, and 557.7 nm in every hour in order to simultaneously monitor the dynamics in both the mesosphere and thermosphere. The exposure times are 3 min at wavelengths of 892.0 nm and 557.7 nm and 5 min at 630.0 nm. It takes roughly 50 min to detect the airglow at three wavelengths during one measurement cycle, and the wind and temperature results at each height are derived at each hour. The data-processing software developed by the HAO, NCAR, is used to derive wind and temperature [*Wu et al*., 2004]. It should be noted that local weather condition such as rain and cloud can seriously degrade the quality of the derived wind and temperature products. The Kelan FPI routinely observes at every night since November 2011, except for an outage from February to April 2013 due to power failure. To date, about 1500 night observations have been accumulated, and over 80% of them passed the data quality criteria [*Yu et al*., 2014].

A meteor radar chain was recently established by the Institute of Geology and Geophysics, Chinese Academy of Sciences [*Yu et al*., 2013]. The meteor radar located at Beijing is manufactured by the Atmospheric Radar Systems of Australia, similar to the Buckland Park meteor radar in Australia and the earlier SKiYMET system in Canada [*Hocking et al*., 2001; *Holdsworth et al*., 2004]. The Beijing MR is designed as an all-sky interferometric meteor wind radar system with a peak power of 7.5 kW, a duty cycle of 10% at a frequency of 38.9 MHz, and a height resolution of typically 1.8 km. The pulse repetition frequency of the radar is 430 Hz. The antenna array consists of six crossed dipoles. A single aerial acts as the transmitter, and five separate aerials, which are configured as an interferometer, act as the receivers. The mean daily meteor count recorded by this meteor radar is about 6000, and almost all meteor echoes appear in the altitude region 70–110 km with the peak counts near 90 km. The echo rates have pronounced diurnal variation, with the peak rates in the early morning hours and smallest rates in the evening hours. Winds in the 70–110 km altitude region could be calculated by detecting the Doppler shift of meteor trails.

Coverage of the FPI and MR stations and data available is shown in Figure 1. The red and blue asterisks indicate the locations of the FPI and MR stations, respectively. The red and blue circles around the two stations denote the maximum ground coverages when the FPI telescope field of view (FOV) and MR radio beam intersect with the MLT region (at the height of 90 km). As shown in Figure 1, the FPI and MR stations are very close to each other and suitable for measurement comparisons. The availability of the FPI and MR observations is shown in the top right of Figure 1. It can be seen that the MR station has a complete record of observations except for a few data gaps. The FPI station has more data gaps due to poor weather conditions. From February to April 2013, no FPI observation was made due to electricity failure at the Kelan station.

The distance between the FPI station at Kelan (38.7°N, 111.6°E) and the MR station at Beijing (40.0°N, 116.4°E) is about 430 km. As the FPI telescope pointing to the northeast direction and the MR radio beam pointing to the southwest direction, the 100 km subpoints of two instruments in the MLT region are less than 200 km apart. This distance is quite small relative to the large-scale of winds in the mesosphere. The FPI spectrometer integrates over the sampling volume and weights the bulk motion of the molecules according to the airglow

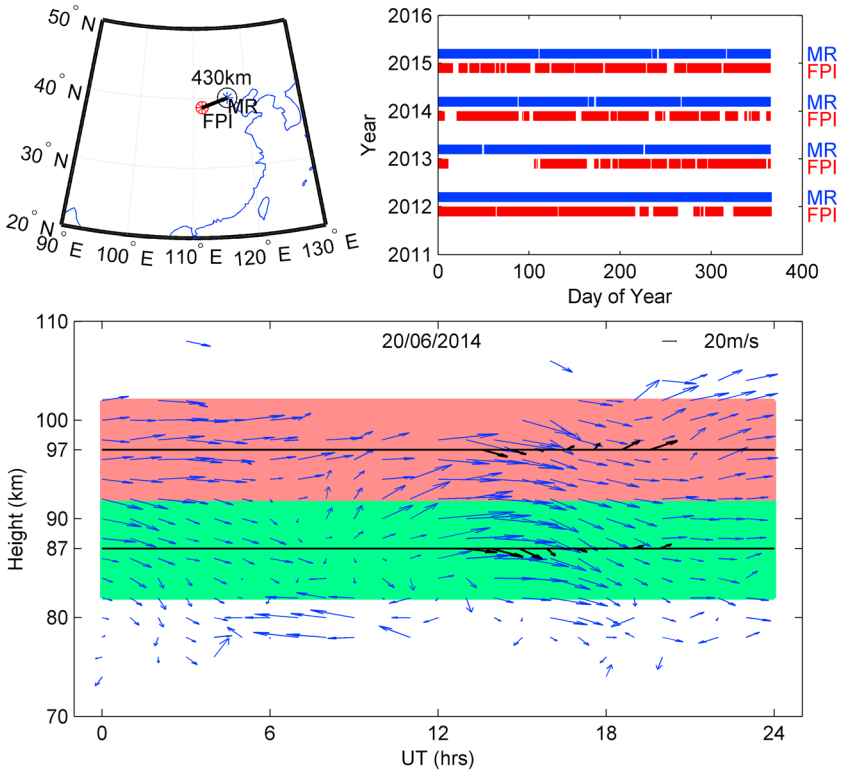


**Figure 1.** (top left) Locations of FPI station at Kelan (111.6°E, 38.7°N) and MR station at Beijing (116.37°E, 39.98°N) and (top right) coverage of FPI and MR database. (bottom) Horizontal winds simultaneously measured by MR (blue arrows) and FPI (black arrows) on 20 June 2014; the green and red boxes are the height-averaged windows, in which the measurements are averaged to represent winds at the heights of 87 km and 97 km, in respectively.

altitudinal distribution of brightness. This distribution usually has a full width at half maximum (FWHM) of about 6–10 km [*O'Brien et al.*, 1965; *Baker and Stair*, 1988]. Therefore, the FPI winds derived from OI (557.7 nm) and OH (892.0 nm) airglows are a weighted averaged winds according to the airglow profiles with a FWHM of about 10 km and peak height at 87 km and 97 km. However, the MR winds, which range from 70 km to 110 km, have a very good height resolution of 2 km, as shown in Figure 1. In order to make a good comparison, the MR winds from height of 82 km to 92 km (green box in Figure 1) and from height of 92 km to 102 km (red box in Figure 1) are first binned and averaged along the height to derive the mean winds at every hour that are representing "height-averaged winds" at 87 km and 97 km, in respectively. Second, the "height-averaged" winds at every hour are then binned and averaged according month and hour to form the "monthly-hourly averaged winds" of MR. Therefore, the monthly-hourly averaged winds, which represent mean winds averaged within a certain height range, are used in the wind data comparison and investigation of the climatology of night winds in the MLT over central China. Since it is generally believed that the geomagnetic disturbance has no obvious influence on the winds in the mesosphere [*Ma et al.*, 2001; *Sivla and Mtumela*, 2012; *Yu et al.*, 2014], data during geomagnetic disturbance are not removed when the monthly-hourly averaged winds are formed in this study.

## 3. Results

When making comparison of the FPI and MR winds, it would be ideal to compare identical period of simultaneous measurement, as well as the monthly-hourly averaged winds. It should be kept in mind that several assumptions when making this comparison: (1) use of the FPI to observe MLT winds ignores the reality that the variation of airglow layer with time and (2) the FPI and MR observe the same bulk of molecules in MLT, which moves with the same speed due to their close distance.

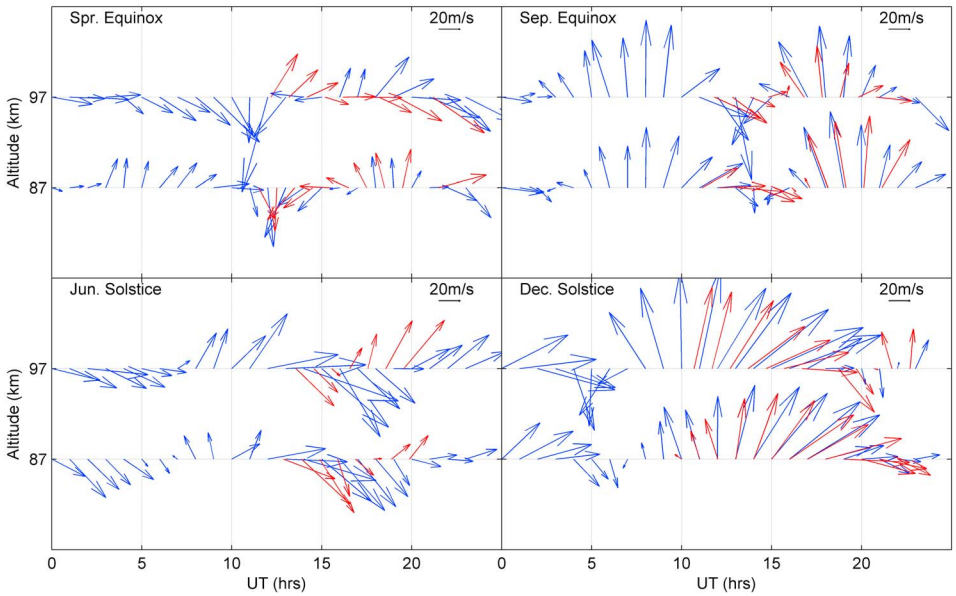


**Figure 2.** Real-time comparison of FPI (red arrows) and MR (blue arrows) winds at spring equinox, June solstice, September equinox, and December solstice in 2014. Very good agreement at September equinox and December solstice, poor agreement at spring equinox and June solstice, and better agreement at the height of 87 km than that at 97 km.

### 3.1. General Comparisons

Figure 2 provides an example of real-time comparison of FPI and MR wind measurements in 2014. Four-day wind data observed on spring equinox, summer solstice, autumn equinox, and winter solstice in 2014 are illustrated. In Figure 2, the MR and FPI winds are seen to rotate uniformly in a clockwise direction with a period of about 24 h and with velocities of 10–50 m/s. The FPI and MR winds show a very good agreement on all the 4 days; the discrepancies between FPI and MR data become slightly large during 11:00–20:00 UT on spring

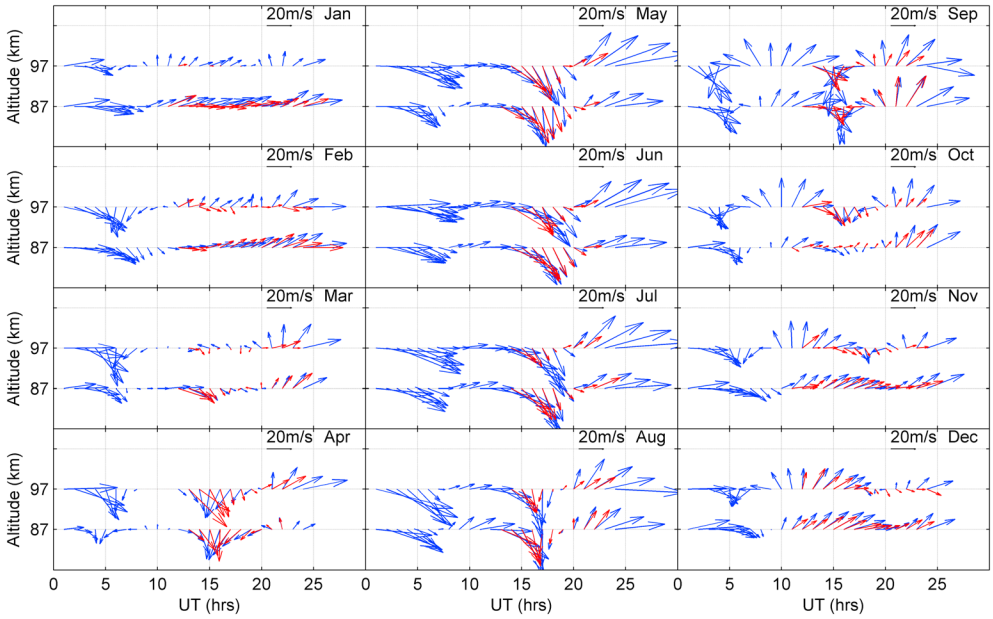


**Figure 3.** Long-term comparison of the monthly-hourly averaged winds of FPI (red arrows) and MR (blue arrows) observations from 2012 to 2014. Very good agreement from May to December, poor agreement from January to March, and better agreement at the height of 87 km than that at 97 km.

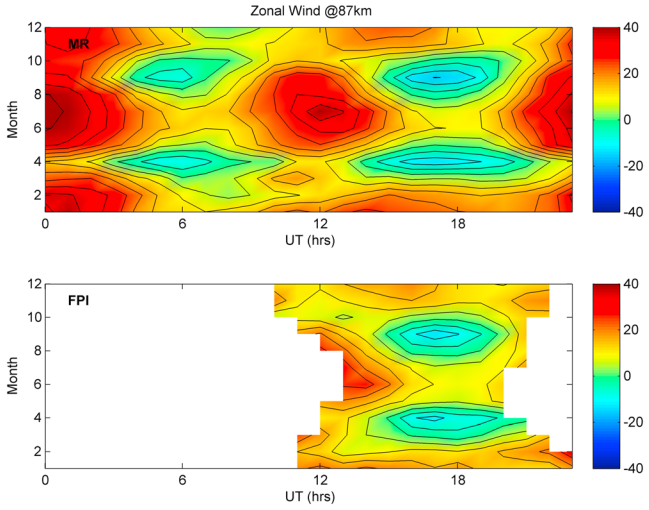


**Figure 4.** The monthly-hourly averaged zonal winds at 87 km derived by the (top) MR and (bottom) FPI data.

equinox and June solstice. The agreement between two instruments is found to be better at the height of 87 km than that at 97 km. The worst agreement is observed at 97 km on spring equinox, namely, all the MR and FPI winds arrows nearly pointing to different directions in most time; only a favorable agreement is at 21:00 UT, but this agreement is unreliable because the errors of FPI wind measurement greatly increased due to dawn degrade the signal-to-noise ratio [*Yu et al.*, 2014].

In order to make a long-term comparison, the monthly-hourly averaged zonal winds of FPI and MR winds observed at the heights of 87 km and 97 km are shown in Figure 3. Similar to that of the real-time comparison in Figure 2, very good agreements between the 4 year averaged FPI and MR winds is shown in Figure 3. Again, better agreement is observed at the height of 87 km than that of 97 km. From April to December, especially from May to August, the winds at both the 87 km and 97 km altitudes show a high degree of consistency as compared to any other months. Obvious discrepancies are observed from January to March. It is found at the altitude of 97 km; major discrepancies are observed after midnight of November and December and during the whole night of January to March.

### 3.2. Wind at the Height of 87 km

Figure 4 shows the monthly-hourly averaged zonal winds at the height of 87 km measured by the FPI (bottom plot) and MR (top plot). The most conspicuous similar features of the FPI and MR zonal winds are the two jet-like westward maxima of winds occurring at around 18:00 UT in equinoctial months. Both the FPI and MR zonal winds are characterized by a strong semiannual variation at 18:00 UT and 06:00 UT with a maximal strength of about −20 m/s in the equinoctial months and by a strong annual variation at 12:00 UT and 00:00 UT with a maximal strength of about 40 m/s in the summer solstice months.

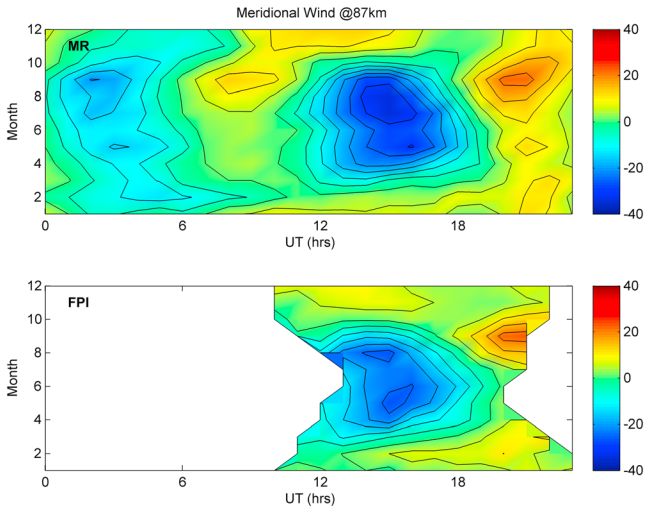


**Figure 5.** The monthly-hourly averaged meridional winds at 87 km derived by the (top) MR and (bottom) FPI data.

Figure 5 shows the monthly-hourly averaged meridional winds at the height of 87 km measured by the FPI and MR. The most notable feature in the MR meridional wind measurements (top plot) and the FPI meridional wind (bottom plot) is an obvious annual variation with a maximal strength of about −40 m/s at around 15:00 UT in the summer months. The FPI and the MR meridional winds are generally southward at around 03:00 UT and 15:00 UT in most months of the year.

In order to obtain the quantitative similarity between the MR and FPI winds, the two-dimensional wind matrix shown in Figure 5 is reshaped into one-dimensional data series. These long-term data series, which

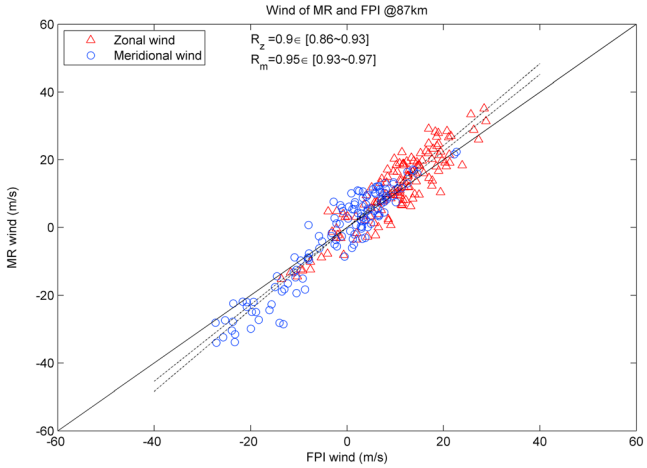


**Figure 6.** The scatterplots of FPI and MR monthly averaged winds at 87 km; the dashed lines indicate the regression line of MR against FPI winds, and the correlation coefficients between measurements and their lower and upper bounds for a 95% confidence interval are shown in top left corner.

are predominant with a semidiurnal variation and very weak annual and semiannual variations, are used to calculate the cross-correlation coefficients between FPI and MR winds. The correlation coefficients between the FPI and MR winds are shown in Figure 6. High correlations are found for both the zonal and meridional winds, namely, with correlation coefficient $R_z = 0.90$ for the zonal wind and $R_m = 0.95$ for the meridional wind. The correlation coefficient of meridional wind is slightly larger than that of zonal wind.

The differences between the day-to-day real-time measured winds and the monthly-hourly averaged winds, which are defined as a root-mean-square error (RMSE) of winds by formula 1, could describe the day-to-day variability averaged in a sense over a year.

$$\mathrm{RMSE}_h = \sum_{i=1}^{N} \sqrt{\frac{\left(W_h^i - W_h^m\right)^2}{N-1}} \tag{1}$$

where $W_h^i$ is the daily wind data measured at the $h$th UT in the $i$th day in a year, $W_h^m$ is the monthly average of all the $W_h^i$ in a year, and $N$ is the number of days in a month. A total of 24 $\mathrm{RMSE}_h$ can be obtained, each corresponding to 01:00 UT hour. As shown in Figure 7, the RMSEs of both the FPI and MR winds have similar amplitudes, most range from 12 m/s to 16 m/s. In the daytime, the RMSEs of MR wind measurements have a weak peak at around 03:00–05:00 UT and trough at around 08:00–10:00 UT. In the nighttime, no obvious temporal variations in RMSE are observed for both the FPI and MR wind data. Overall, the RMSE of MR zonal wind is larger than that of MR meridional wind.

### 3.3. Winds at the Height of 97 km

The monthly-hourly averaged zonal winds at 97 km derived from the FPI (bottom plot) and MR (top plot) data are illustrated in Figure 8. General similarity between the FPI and MR winds could be found in Figure 8, but the differences are more significant than those at 87 km as shown in Figure 4. The FPI zonal wind shown in the bottom plot of Figure 8 shows two jet-like westward maxima in the equinoctial months, and it is characterized by a semiannual variation occurring at around 18:00 UT with magnitudes not higher than −15 m/s. In the top plot of Figure 8, the MR zonal wind data have a very weak asymmetric semiannual variation, and their amplitudes are relatively smaller than the MR winds at 87 km. A strong annual variation of the MR wind, which has a maximal strength of about 40 m/s, is pronounced at 12:00 UT and 00:00 UT in summer solstice months.

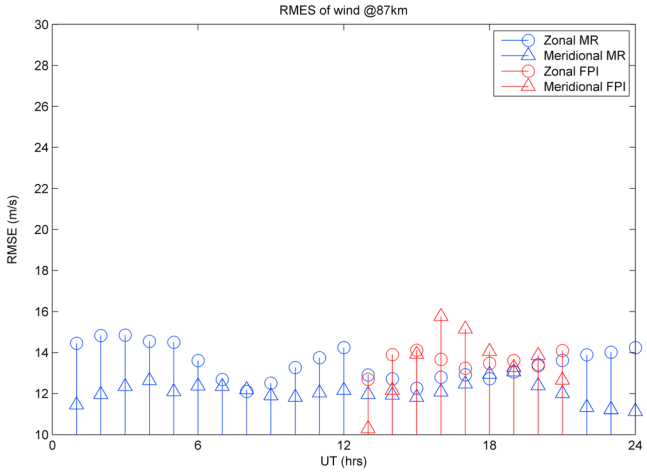


**Figure 7.** Daily variation of the root-mean-square error (RMSE) of monthly-hourly averaged winds at 87 km.

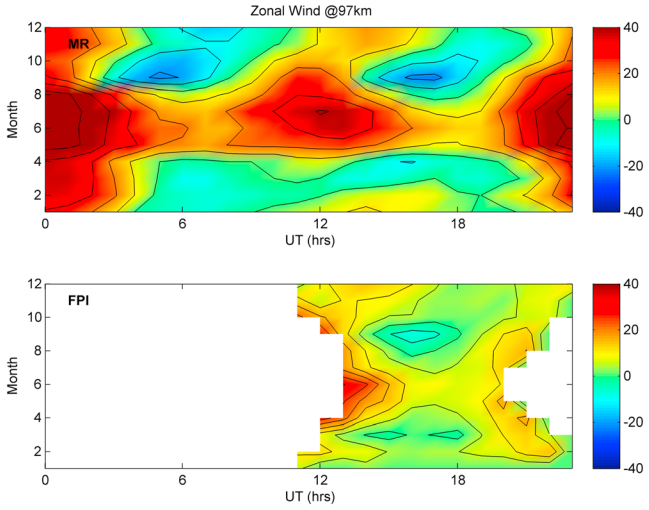


**Figure 8.** The monthly-hourly averaged zonal winds at 97 km derived by the (top) MR and (bottom) FPI data.

The monthly-hourly averaged meridional wind measurements at 97 km are very similar to those at 87 km. First, the annual variation is still notable at around 15:00 UT. The southward wind reaches maximal strength of about 40 m/s at around 15:00 UT in summer months. Another weak semiannual variation of southward wind reaches maximal strength of about −40 m/s at 03:00–04:00 UT in both spring and autumn equinoctial months. In the rest time, the meridional wind is generally northward without pronounced annual variation (Figure 9).

As demonstrated in Figure 10, the correlation coefficients between measurements at the height of 97 km are about 0.86 for meridional wind and 0.73 for zonal wind. It is apparent that the meridional correlation coefficients are slightly higher than those of zonal winds. The correlation coefficients at 97 km are generally smaller than those at 87 km.

Figure 11 shows the temporal variations of the FPI and MR wind RMSEs at 97 km. In general, the RMSEs of FPI and MR winds, which are in the range of 10~18 m/s and 15~21 m/s, respectively, are approximately in the same amplitude. The most notable feature of Figure 11 is a minimal RMSE occurring at around 08:00–12:00 UT for both zonal and meridional winds, like the wind RMSE at the height of 87 km in Figure 7. Moreover, there are RMSE peaks around 03:00–05:00 UT and troughs around 08:00–10:00 UT, which are more pronounced than those at 87 km. In general, the RMSEs of both MR and FPI winds at 97 km are slightly higher than those at 87 km. No obvious temporal dependence of the RMSE is found in the nighttime.

## 4. Discussions

Our comparisons in general show a very good agreement between the FPI and MR wind measurements, which are consistent with the previous studies such as *Phillips et al.* [1994]. But some discrepancies between FPI and MR winds are apparent, and these discrepancies seem to be height and geomagnetic field dependent. First, according to the real-time comparison in Figure 2 and the long-term comparison in Figure 3, better agreements are found at the height of 87 km than that at the height of 97 km. Second, according to the scatterplots of FPI and MR wind measurements in Figures 6 and 10, the correlation coefficients of long-term FPI and MR winds have obviously different magnitudes at two altitudes (87 km and 97 km) and in two directions (meridional and zonal). The correlation coefficients of long-term FPI and MR data at 87 km are higher than 97 km, and correlation coefficient of the meridional wind is higher than

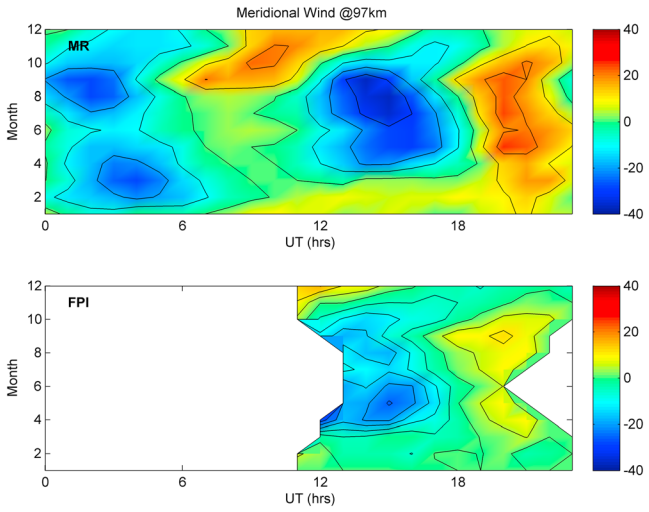


**Figure 9.** The monthly-hourly averaged meridional winds at 97 km derived by the (top) MR and (bottom) FPI data.

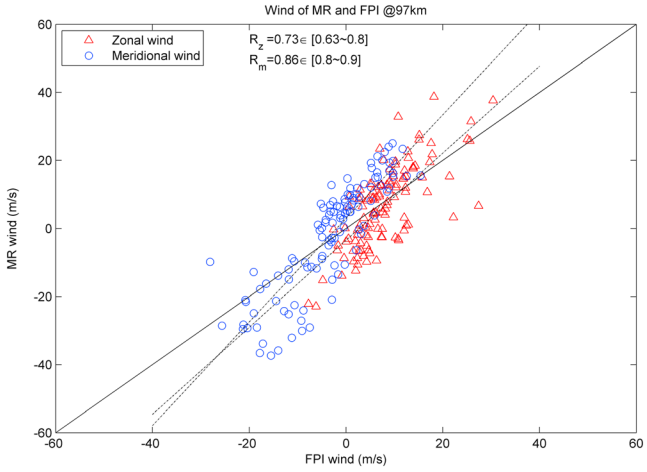


**Figure 10.** The scatterplots of FPI and MR monthly averaged winds at 97 km; the dashed lines indicate the regression line of MR against FPI winds, and the correlation coefficients between measurements and their lower and upper bounds for a 95% confidence interval are shown in top left corner.

the zonal wind. Without other measurements, it is however difficult to tell which one has more reasonable measurements, because it is impossible to determine the "true" winds in the atmosphere. In the following, all the possible reasons that could lead to those discrepancies are to be discussed.

### 4.1. Variation of Peak Height and FWHM of Airglow Layers

The variations of the height and profile shape of airglow layers should be considered as primary cause of the differences between MR and FPI winds, particularly for the winds measured by FPI at the height of 97 km. It is well known that the FPI spectrometer integrates over the sampling volume and weights the bulk motion of the molecules according to the airglow distribution of brightness with height [*Wu et al*., 2004]. Previous studies showed that the airglow layer distributed at altitudes with a peak at the height of 87 km (for OH 892.0 nm) and 97 km (for OI 557.7 nm) and with a FWHM about 6–10 km [*O'Brien et al*., 1965; *Yee and Abreu*, 1987; *Baker and Stair*, 1988]. Recent investigations also reported a significant variation of airglow peak height up to several kilometers with longitudinal, latitudinal, diurnal, and seasonal variations [*Shepherd et al*., 1993; *Phillips et al*., 1994; *Plagmann et al*., 1998; *Zhang and Shepherd*, 1999; *Russell et al*., 2005]. Many authors also noticed that the variation of profile of airglow may have considerable influence on the interpretation of wind measurements by FPI. *Fujii et al*. [2004] attributed the observed differences between MU meteor radar winds and FPI winds to the vertical shift of the green line layer height caused by gravity wave. Meriwether and Larsen [in his presentation, 2014] pointed out that the green line wind speed measured by FPI is always much less than the maximum speed or considerably greater than the minimum speed due to strong shear in horizontal winds existing within the OI volume emission profile. In our views, the variations of airglow profile as well as the turbulent shear in the MLT probably have a combined effect on the FPI measurements and lead to discrepancies between FPI and MR measurements.

In order to make clear how the variation of airglow layer peak height and FWHM influence on the discrepancies of MR and FPI wind measurements, a new data analysis method is introduced. When deriving the height-averaged MR winds at the heights of 87 km and 97 km (as shown in the bottom plot of Figure 1), a Gaussian distribution weight coefficient, which is similar to the "real profile" of airglow layer, is introduced instead of the old uniform weight coefficient described in section 2 of this paper. The weight coefficient is defined as

$$f(h) = \frac{1}{\sqrt{2\pi}\sigma}\exp\left(-\frac{(h-h_p)^2}{2\sigma^2}\right) \quad (2)$$

where $f(h)$ varies as a Gaussian-shape function with a peak height of $h_p$ and a FWHM of $\sigma$ when the $h$ ranges from 70 km to 110 km. In the following

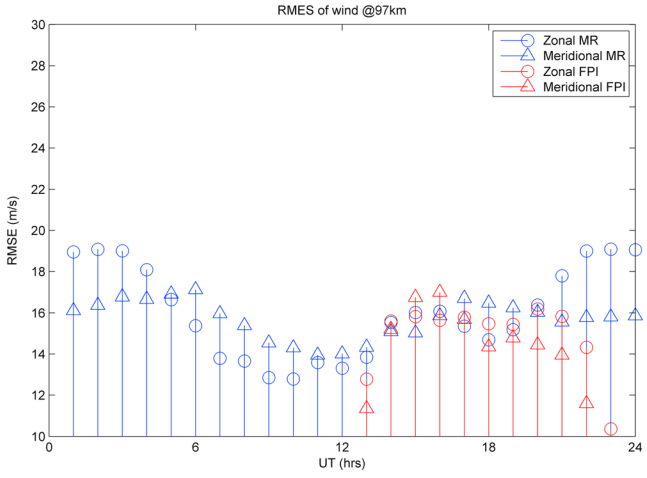


**Figure 11.** Daily variation of the root-mean-square error (RMSE) of monthly-hourly averaged winds at 97 km.

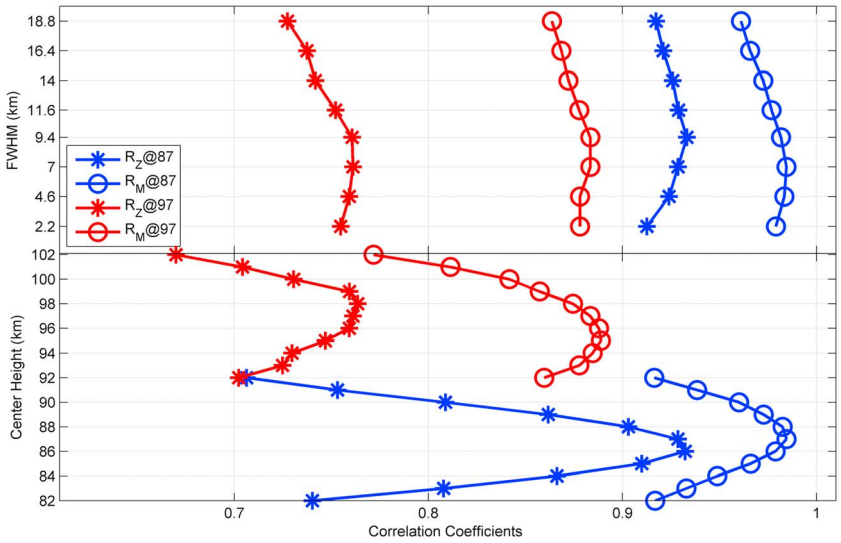


**Figure 12.** The correlation coefficients between the MR and FPI winds as a function of (top) FWHM ($\sigma$) and (bottom) peak height ($h_p$) of airglow layer; the blue and red lines are the correlation coefficients of winds at the heights of 87 km and 97 km, and the lines with circles and asterisks are the correlation coefficients of winds in meridional and zonal directions.

studies, the $h_p$ arbitrarily varies from 82 km to 92 km to simulate the peak height variation of 892.0 nm airglow and varies from 92 km to 102 km to simulate the peak height variation of 557.7 nm airglow with a step interval of 1 km. The $\sigma$ arbitrarily varies from 2.2 km to 18.8 km with a step interval of 2.4 km to simulate the variation of FWHM.

The correlation coefficients between MR and FPI winds, as a function of the $h_p$ and $\sigma$, are shown in Figure 12. In both plots, the blue and red lines represent the correlation coefficients between the MR and FPI winds at the heights of 87 km and 97 km, respectively. The lines with circles and asterisks represent the correlation coefficients between MR and FPI winds in meridional and zonal directions, respectively. From the top plot of Figure 12, all correlation coefficient profiles rise slowly and then drop with the FWHM varying from 2.2 km to 18.8 km. From the bottom plot of Figure 12, it is noted that the profiles of correlation coefficients versus peak height are much sharper than those profiles versus FWHM, which implies that the correlation coefficient are more sensitive to changes of peak height than that of FWHM. The correlation coefficients rise quickly and then drop with the peak heights in the range of 82 km and 92 km (corresponding to 892.0 nm airglow layer) and in the range of 92 km to 102 km (corresponding to 557.7 nm airglow layer). The relative deviation of peak-to-trough correlation coefficient, which is defined as below, is calculated from the eight profiles in Figure 12 and is listed in Table 1.

$$P2T = \frac{\max(\text{correlation coefficient}) - \min(\text{correlation coefficient})}{\min(\text{correlation coefficient})} \times \% \tag{3}$$

According to Table 1, it is clear that variation of peak height ($h_p$) could on average lead to the relative deviation of peak-to-trough correlation coefficient ($P2T$) as high as about 20% at the height of 87 km and about 14.8% at the height of 97 km. In contrast, the influence of variation of FWHM ($\sigma$) is much smaller, which is about 2.4% and 3.5% at the height of 87 km and 97 km, respectively.

**Table 1.** The Relative Deviations of Peak-to-Trough Correlation Coefficient ($P2T$, in Unit of %) Versus Peak Height and FWHM Derived From Figure 12

| Profiles | | | | | | |
|---|---|---|---|---|---|---|
| Parameter | $R_m$ at 87 km | $R_z$ at 87 km | $R_m$ at 97 km | $R_z$ at 97 km | Mean Deviation at 87 km | Mean Deviation at 97 km |
| $h_p$ | 7.5 | 32.4 | 15.4 | 14.2 | 20.0 | 14.8 |
| $\sigma$ | 2.5 | 2.3 | 2.3 | 4.7 | 2.4 | 3.5 |

**Table 2.** "Best" Peak Height and FWHM (in Unit of km) Correspond to Maximal Correlation Coefficient *d* Profiles

| Height and Width | $R_m$ at 87 km | $R_z$ at 87 km | $R_m$ at 97 km | $R_z$ at 97 km | Mean Height at 87 km | Mean Height at 97 km |
|---|---|---|---|---|---|---|
| $h_p$ | 87 | 86 | 95 | 98 | 86.5 | 96.5 |
| $\sigma$ | 7 | 9.4 | 9.4 | 8 | 8.2 | 8.7 |

Moreover, according to Figure 12, the "best" FWHM and peak height, which correspond to the maximal correlation coefficient, could be derived and shown in Table 2.

As shown in Table 2, the best mean peak height ($h_p$) and FWHM ($\sigma$), which are derived from 4 year data comparison between MR and FPI measurements, are about 86.5 km and 8.2 km, respectively, for OH airglow (892.0 nm) and 96.5 km and 8.7 km, respectively, for OI airglow (557.7 nm). These results are generally consistent with the theory [*Peterson et al*., 1966] and other results [*O'Brien et al*., 1965; *Gulledge et al*., 1968; *Yee and Abreu*, 1987; *Baker and Stair*, 1988].

### 4.2. The Effect of Geomagnetic Field

It is generally believed that the charged particles in meteor trail, which are composed of $Fe^+$, $Mg^+$, $Si^+$, and $Na^+$, can be fully collided by neutral particles and moved at the same speed and in the same direction as the neutral particles do. When measuring the motion of neutral particles in the upper atmosphere by MR, the plasmas in the ionized trail, which is a very good reflection medium for radio radar wave, are usually taken as an ideal target by radio radar instead of neutral particles. However, the assumption of same speed of neutral and ionized particles does not always hold true. As the height increase, the numbers of neutral molecules gradually decrease and the collision between neutral and charged particles become less frequent. Therefore, the effect of other forces on charged particles, i.e., electric field and geomagnetic field, although relatively smaller in middle latitudes, could not be completely ignored and may affect the movement of charged particles at higher altitudes. However, the neutral particles may be free from these electric and geomagnetic forces. Therefore, the movements of charged particles may differ from the neutral ones. When using MR radar to measure wind, a basic assumption is that the motion of plasmas in the ionized trail was assumed to move in the same speed and direction as the neutral atmospheric molecules do. However, as the increase of height, the collision force of neutral particles on charged particles rapidly decreases, and the drag force of geomagnetic and fields on charged particles slightly decrease; therefore, the charged particles would move at different speed and direction from the neutral molecules. Therefore, MR wind derived from meteor ionized trail may be not reliable as the height increasing.

*Reid* [1983] pointed out that influence of electric fields on radar-measured winds in the upper mesosphere may be serious; in that, velocities of plasmas irregularities detected by radio radar may depart significantly from neutral wind vectors, especially at auroral zone latitudes. Although the electric field are relative smaller in middle latitudes, the electric and geomagnetic forces on charged particles in meteoroid could not be completely ignored and may have some influence on MR wind measurements at higher altitudes. It could lead to the differences of correlation coefficient between MR and FPI measurements shown in Figures 6, 10, and 12, which is much higher at the altitude of 87 km than that at 97 km and is much higher in the meridional component than in the zonal component. This difference very likely arises from combined effects of electric and geomagnetic fields in the MLT.

Following the momentum equation by *Rishbeth and Garriott* [1969], *Zhou* [2015] investigated the latitudinal and altitudinal variations of the charged particles motion under driving of neutral winds as well as real electric and geomagnetic fields. They found that the difference of motion between charged and neutral particles became larger as the latitude and height increased. Simulation was conducted at Beijing station to study the impact of electric and geomagnetic fields on wind speed. Their simulation results showed that velocity difference between neutral and charged particles was about 0.2% at the height of 86 km and the difference increased to 0.8% at the height of 98 km. The simulation parameters, which referred from *Xiong et al*. [2004], were given as the following: the zonal wind speeds 30 m/s, meridional wind speed 10 m/s, the vertical winds speed 0.1 m/s, the eastward electric fields 1 mV/m, the southward electric fields −5 mV/m, and the

geomagnetic field derived from International Geomagnetic Reference Field 2000. This simulation can partially account for difference of correlation coefficients at 87 km and 97 km.

Moreover, the correlation coefficients of zonal wind, which are clearly smaller than that of meridional wind at both heights, are another interesting characteristic shown in Figures 6 and 10. Unfortunately, this difference was not found in Zhou's simulation; namely, the velocity difference between neutral and charged particles did not seem to be dependent on geomagnetic field direction according to *Zhou* [2015]. On the other hand, a number of theoretical papers reported that geomagnetic field inhibits cross-field diffusion of meteor trail, particularly at high altitudes [*Kaiser et al*., 1969; *Jones*, 1991; *Dyrud et al*., 2001]. When estimating the ambipolar diffusion coefficient, *Lee et al*. [2013] included meteors only below 90 km to avoid possible geomagnetic effects. According their views, we speculate that the inhibition of ions in meteor trails across the geomagnetic field can partially account for the difference of correlation coefficients in zonal and meridional winds. In this assumption, the zonal winds measured by MR, which are perpendicular to geomagnetic field, would be affected more by geomagnetic fields than the meridional winds measured by MR, which are partly parallel to geomagnetic field over Beijing station (40.0°N, 116.4°E; geomagnetic inclination is about 58.3°). However, it is completely different for the wind measured by FPI. The FPI detects the neutral motions by measuring the airglow Doppler shift of neutral molecules in the atmosphere, and it is not affected by the geomagnetic field.

The geomagnetic field could very likely have serious inhibition of the vertical movement and have no influence on parallel movement of charged particles in meteoroid. Therefore, the MR zonal winds, which are derive from tracking the perpendicular movement of charged particles in meteoroid and are most seriously influenced by geomagnetic field, could depart from the movement of neutral molecules, leading to a smallest zonal correlation coefficient between measurements. The MR meridional winds, which are derived from tracking the parallel movement of charged particles in meteoroid and are not influenced by geomagnetic field, could have movement very similar to neutral molecules, leading to a largest meridional correlation coefficient between measurements.

### 4.3. Other Possibility

The numbers of observed meteoroid-ionized trail usually reach their maximal value at the height of 90 km, which would lead to a more reliable and accurate winds derived by MR at around this height and a less accurate winds at other height away from 90 km [*Hocking*, 1997; *Kumar et al*., 2007]. The height of maximal meteors number observed in Beijing MR is about 91 km, and the number of observed meteors diminishes as an exponent function up to 110 km. A real-time meteor event detected by the MR over Beijing station can be found at http://space.iggcas.ac.cn/Meteoradar.html. For this reason, the occasional lack of enough numbers of meteor trails at the height of 97 km can be partially responsible for the difference in correlation coefficient.

The relatively pronounced discrepancies observed from January to March in Figure 3 could be associated with the following reasons: (1) in the first winter of observation at Kelan, there was serious water vapor contamination on the glass dome due to the large-temperature differences inside and outside of observation room, which would result in extra bias in the FPI-derived wind measurements. In the recent years, a calorifier was used to blow the dome to inhibit the formation of water vapor. (2) The lack of FPI measurement during these months is shown in the right plot of Figure 1. There was a long-term gap of FPI measurement in 2013 due to a failure of electric power [*Yu et al*., 2014]. The lack of data may lead to large deviation of monthly-hourly averaged winds.

As shown in Figure 11, the daily course of root-mean-square error (RMSE) of MR winds, which are in different amplitudes at the heights of 87 km and 97 km, can be due to different amplitudes of tides and atmospheric gravity wave (AGW) at these heights. Generally, the daily variation of AGW, which could lead to the day-to-day variability of MR winds, should be partly responsible for this temporal variation as shown in Figure 11. *Ding et al*. [2011] found that AGW occurrence in central China also had a semidiurnal variation. One peak was at around 12:00 LT (04:00 UT), another was at around 24:00 LT (16:00 UT), and two troughs were at around 08:00 LT (00:00 UT) and 18:00 LT (10:00 UT). In their views, the peak AGW at 12:00 LT (04:00 UT) was attributed to the perturbation from lower atmosphere, which could lead to maximal RMSE at around 04:00 UT in Figures 7 and 11. The trough of AGW at around 08:00 LT and 18:00 LT also could lead to minimal RMSE at around 10:00 UT in Figures 7 and 11. The second peak of AGW at around 24:00 LT (16:00 UT) was

attributed to the electrodynamic process caused by plasma instability in the *F* layer, which is not related with the AGW in lower atmosphere.

## 5. Summary

Over 4 year wind observations collected by FPI and MR over two adjacent stations in central China are used to investigate the wind climatology in MLT and to made comparison with these different instruments. In general, the FPI and MR wind measurements have very good agreements between each other, but some discrepancies remain in the zonal wind and at the higher altitudes. Main results are summarized as follows:

1. The 4 year monthly-hourly averaged winds from 2012 to 2015 show that the FPI and MR winds generally fit very well with each other from April to December, especially from May to August. Some discrepancies are observed from January to March, which could be attributed to serious water vapor contamination on the glass dome during the first year of observation, as well as the lacking of FPI measurement during these months in 2013.
2. At the altitude 87 km, the monthly-hourly mean wind vectors show that the FPI and MR winds agree with each other well in all months. Moreover, both the FPI and MR zonal winds have an obvious semiannual variation with a maximal strength of −20 m/s at around 18:00 UT in equinoctial month. The meridional winds have an obvious annual variation with a maximal strength of −40 m/s at around 15:00 UT in summer months. The correlation coefficients between the FPI and MR winds are as high as 0.95 for meridional wind and 0.90 for zonal wind. The root-mean-square error (RMSE) of zonal and meridional winds ranges from 12 m/s to 16 m/s for both the FPI and MR.
3. At the altitude 97 km, monthly-hourly mean wind field vectors show that FPI and MR winds agree with each other well from May to October, but obvious differences exists in the rest months. Moreover, very weak semiannual variation at around 18:00 UT could be found from both the FPI and MR zonal winds, but the annual variation at around 15:00 UT is pronounced for FPI and MR meridional winds. The correlation coefficients between the FPI and MR winds are 0.86 for meridional wind and 0.73 for zonal wind, which are smaller than that of winds at 87 km. The root-mean-square error (RMSE) of winds range from 10 to 18 m/s and 15 to 21 m/s for FPI and MR winds, respectively.
4. The correlation coefficients between the FPI and MR winds, which are higher for the meridional wind than the zonal wind and higher at 87 km than at 97 km, are difficult to explain because many factors can lead to differences between the MR and FPI measurements. The variation of the height and profile shape of airglow layers, the effect of Earth's magnetic field on meteor-ionized particles, the relatively less meteoroids observed at the height of 97 km, and the propagation of gravity waves could be responsible for the differences between the FPI and MR measurements.

A Gaussian distribution weight coefficient is used to calculate the height-averaged winds at 87 km and 97 km instead of the old uniform weight coefficient, with which variations of the new correlation coefficients with peak height and FWHM of airglow are investigated by shifting the peak height and FWHM. It is found that variation of peak height could lead to a change of about 20% in relative deviation of peak-to-trough correlation coefficient at the height of 87 km and about 14.8% at the height of 97 km on average. The variation of FWHM can lead to a smaller change in relative deviation of peak-to-trough correlation coefficient, about 2.4% and 3.5% at the heights of 87 km and 97 km, respectively. The best estimate of peak height and FWHM, which correspond to maximum correlation coefficient between MR and FPI measurements, are about 86.5 km and 8.2 km for OH airglow (892.0 nm) and 96.5 km and 8.7 km for OI airglow (557.7 nm), respectively.

It should be noted that both MR and FPI are very useful instruments for wind measurement in the upper atmosphere. Any expectation of exact consistency between these measurements is not realistic. One should notice that different techniques are involved in each instrument when using these data.

**Acknowledgments**

We deeply appreciated the helpful discussion with J.H. Lei at the University of Science and Technology of China and J.G. Xiong at the Institute of Geology and Geophysics, Chinese Academy of Sciences. We also are grateful to the National Center for Space Weather, China Meteorological Administration, and Beijing National Observatory of Space Environment, Chinese Academy of Sciences, and the China Meridian Project, for kindly providing the FPI and MR data. Huang (Huangc@cma.gov.cn) and Hu (hulh@mail.iggcas.ac.cn) would like to provide FPI data and MR data, respectively. This work was supported by the National Natural Science Foundation of China (grants 41274159, 41574147, and 41231065). National Key Basic Research Program of China (2012CB825604). Zhizhao Liu thanks the support by the Hong Kong Research Grants Council General Research Fund project PolyU 5203/13E (B-Q37X).

## References

Ammosov, P. P., and G. Gavrilyeva (2008), Study of the semidiurnal tide derived from observations of OH(6,2) and O2(0-1) nightglow at high latitudes, in *Proceedings of 33rd Annual European Meeting on Atmospheric Studies by Optical Methods*, *IRF Sci. Rep.*, vol. 292, pp. 43–48, Swedish Institute of Space Physics, Kiruna, Sweden.

Aruliah, A. L., E. M. Griffin, A. D. Aylward, E. A. K. Ford, M. J. Kosch, C. J. Davis, V. S. C. Howells, S. E. Pryse, H. R. Middleton, and J. Jussila (2005), First direct evidence of meso-scale variability on ion-neutral dynamics using co-located tristatic FPIs and EISCAT radar in northern Scandinavia, *Ann. Geophys.*, *23*, 147–162, doi:10.5194/angeo-23-147-2005.

Baker, D. J., and A. T. Stair Jr. (1988), Rocket measurements of the altitude distribution of the hydroxyl airglow, *Phys. Scr.*, *37*(4), 611–622, doi:10.1088/0031-8949/37/4/021.

Cervera, M. A., and I. M. Reid (2000), Comparison of atmospheric parameters derived from meteor observations with CIRA, *Radio Sci.*, *35*(3), 833–843, doi:10.1029/1999RS002226.

David, M., J. J. Sojka, R. W. Schunk, and J. M. Holt (2013), The neutral wind in ionospheric modeling: The month-long ISR campaign at millstone hill, October 2002, Abstract SA41B-2115 presented at 2013 Fall Meeting, AGU, San Francisco, Calif., Dec.

Ding, F., W. Wan, G. Xu, T. Yu, G. Yang, and J. Wang (2011), Climatology of medium-scale traveling ionospheric disturbances observed by a GPS network in central China, *J. Geophys. Res.*, *116*, A09327, doi:10.1029/2011JA016545.

Dyrud, L. P., M. M. Oppenheim, and E. A. F. Vom (2001), The anomalous diffusion of meteor trails, *Geophys. Res. Lett.*, *28*(14), 2775–2778, doi:10.1029/2000GL012749.

Emmert, J. E., B. G. Fejer, and D. P. Sipler (2003), Climatology and latitudinal gradients of quiet time thermospheric neutral winds over Millstone Hill from Fabry-Perot interferometer measurements, *J. Geophys. Res.*, *108*(A5), 1196, doi:10.1029/2002JA009765.

Emmert, J. T., M. L. Faivre, G. Hernandez, M. J. Jarvis, J. W. Meriwether, R. J. Niciejewski, D. P. Sipler, and C. A. Tepley (2006), Climatologies of nighttime upper thermospheric winds measured by ground-based Fabry-Perot interferometers during geomagnetically quiet conditions: 1. Local time, latitudinal, seasonal, and solar cycle dependence, *J. Geophys. Res.*, *111*, A12302, doi:10.1029/2006JA011948.

Fejer, B. G., J. T. Emmert, and D. P. Sipler (2002), Climatology and storm time dependence of nighttime thermospheric neutral winds over Millstone Hill, *J. Geophys. Res.*, *107*(A5), 1052, doi:10.1029/2001JA000300.

Forbes, J. M., N. A. Makarov, and Y. I. Portnyagin (1995), First results from the meteor radar at South Pole: A large 12-hour oscillation with zonal wavenumber one, *Geophys. Res. Lett.*, *22*(23), 3247–3250, doi:10.1029/95GL03370.

Fritts, D. C., D. Janches, H. Iimura, W. K. Hocking, J. V. Bageston, and N. M. P. Leme (2012), Drake Antarctic Agile Meteor Radar first results: Configuration and comparison of mean and tidal wind and gravity wave momentum flux measurements with Southern Argentina Agile Meteor Radar, *J. Geophys. Res.*, *117*, D02105, doi:10.1029/2011JD016651.

Fujii, J., T. Nakamura, T. Tsuda, and K. Shiokawa (2004), Comparison of winds measured by MU radar and Fabry-Perot interferometer and effect of OI 5577 airglow height variations, *J. Atmos. Terr. Phys.*, *66*(6–9), 573–583, doi:10.1016/j.jastp.2004.01.010.

Fuller-Rowell, T., M. Codrescu, N. Maruyama, M. Fredrizzi, E. Araujo-Pradere, S. Sazykin, and G. Bust (2007), Observed and modeled thermosphere and ionosphere response to superstorms, *Radio Sci.*, *42*, RS4S90, doi:10.1029/2005RS003392.

Fuller-Rowell, T. J. (1995), The dynamics of the lower thermosphere, in *Upper Mesosphere and Lower Thermosphere: A Review of Experiment and Theory*, edited by R. M. Johnson and T. L. Killeen, pp. 23–36, AGU, Washington, D. C.

Gulledge, I. S., D. M. Packer, S. G. Tilford, and J. T. Vanderslice (1968), Intensity profiles of the 6300-A and 5577-A OI lines in the night airglow, *J. Geophys. Res.*, *73*(17), 5535–5547, doi:10.1029/JA073i017p05535.

Hernandez, G., and R. G. Roper (1979), A comparison between radio meteor and airglow winds, *J. Geomagn. Geoelectr.*, *31*(3), 419–426, doi:10.5636/jgg.31.419.

Hocking, W. K. (1997), Recent advances in radar instrumentation and techniques for studies of the mesosphere, stratosphere, and troposphere, *Radio Sci.*, *32*, 2241–2270, doi:10.1029/97RS02781.

Hocking, W. K., B. Fuller, and B. Vandepeer (2001), Real-time determination of meteor related parameters utilizing modern digital technology, *J. Atmos. Sol.-Terr. Phys.*, *63*, 155–169, doi:10.1016/S1364-6826(00)00138-3.

Holdsworth, D. A., I. M. Reid, and M. A. Cervera (2004), Buckland Park all-sky interferometric meteor radar, *Radio Sci.*, *39*, RS5009, doi:10.1029/2003RS003014.

Ishii1, M., S. Oyama, S. Nozawa, R. Fujii, E. Sagawa1, S. Watari, and H. Shinagawa (1999), Dynamics of neutral wind in the polar region observed with two Fabry-Perot interferometers, *Earth Planets Space*, *51*, 833–844, doi:10.1186/BF03353242.

Jiang, G.-Y. J.-G. X., W.-X. Wan, B.-Q. Ning, L.-B. Liu, R. A. Vincent, and I. Reid (2005), The 16-day waves in the mesosphere and lower thermosphere over Wuhan (30.6°N, 114.5°E) and Adelaide (35°S, 138°E), *Adv. Space Res.*, *35*(11), 2005–2010, doi:10.1016/j.asr.2005.03.011.

Jiang, G.-Y., J. Y. Xu, W. Yuan, B. Q. Ning, W. X. Wan, and L. H. Hu (2012), A comparison of mesospheric winds measured by FPI and meteor radar located at 40°N, *Sci. China Technol. Sci.*, *55*(5), 1245–1250, doi:10.1007/s11431-012-4773-1.

Jones, W. (1991), Theory of diffusion of meteor trains in the geomagnetic field, *Planet. Space Sci.*, *39*(9), 1283–1288, doi:10.1016/0032-0633(91)90042-9.

Kaiser, T. R., W. M. Pickering, and C. D. Watkins (1969), Ambipolar diffusion and motion of ion clouds in the Earth's magnetic field, *Planet. Space Sci.*, *17*(69), 519–552, doi:10.1016/0032-0633(69)90083-X.

Kumar, K. K., G. Ramkumar, and S. T. Shelbi (2007), Initial results from SKiYMET meteor radar at Thumba (8.5°N, 77°E): 1. Comparison of wind measurements with MF spaced antenna radar system, *Radio Sci.*, *42*, RS6008, doi:10.1029/2006RS003551.

Langille, J. A., W. E. Ward, S. Alan, and D. L. Arsenault (2013), Wind observations with imaging field-widened Michelson interferometers, *Appl. Opt.*, *52*(8), 1617–1628, doi:10.1364/AO.52.001617.

Lee, C. S., J. P. Younger, I. M. Reid, Y. H. Kim, and J. H. Kim (2013), The effect of recombination and attachment on meteor radar diffusion coefficient profiles, *J. Geophys. Res. Atmos.*, *118*, 3037–3043, doi:10.1002/jgrd.50315.

Lloyd, N., A. H. Manson, D. J. McEwen, and C. E. Meek (1990), A comparison of middle atmospheric dynamics at Saskatoon (52°N, 107°W) as measured by a medium-frequency radar and a Fabry-Perot interferometer, *J. Geophys. Res.*, *95*, 7653–7660, doi:10.1029/JD095iD06p07653.

Ma, G., K. Igarashi, and K. Hocke (2001), Mid-latitude winds in the mesosphere: A superposed epoch analysis over the geomagnetic storm times, *J. Atmos. Terr. Phys.*, *63*, 1993–2001, doi:10.1016/S1364-6826(01)00064-5.

Manning, L. A., O. G. Villard, and A. M. Peterson (1950), Meteoric echo study of upper atmosphere winds, *Proc. IRE*, *38*(8), 877–883, doi:10.1109/JRPROC.1950.234124.

Meriwether, J. W. (2006), Studies of thermospheric dynamics with a Fabry-Perot interferometer network: A review, *J. Atmos. Terr. Phys.*, *68*, 1576–1589, doi:10.1016/j.jastp.2005.11.014.

O'Brien, B. J., F. R. Allum, and H. C. Goldwir (1965), Rocket measurement of midlatitude airglow and particle precipitation, *J. Geophys. Res.*, *70*(1), 161–175, doi:10.1029/JZ070i001p00161.

Peterson, V. L., T. E. VanZandt, and R. B. Norton (1966), F-region nightglow emissions of atomic oxygen: 1. Theory, *J. Geophys. Res.*, *71*(9), 2255–2265, doi:10.1029/JZ071i009p02255.

Phillips, A., A. H. Manson, C. E. Meek, and E. J. Llewell (1994), A long-term comparison of middle atmosphere winds measured at Saskatoon (52°N, 107°W) by a medium-frequency radar and a Fabry-Perot interferometer, *J. Geophys. Res.*, *99*, 12,923–12,935, doi:10.1029/94JD00618.

Plagmann, M., S. H. Marsh, W. J. Baggaley, R. G. T. Bennett, K. A. Deutsch, G. J. Fraser, G. Hernandez, B. N. Lawrence, G. E. Plank, and R. W. Smith (1998), Annual variation of airglow heights derived from wind measurements, *Geophys. Res. Lett.*, *26*, 4457–4460, doi:10.1029/1998GL900212.

Rees, D., P. J. Charleton, N. Lloyd, R. W. Smith, F. G. McCormac, and A. Steen (1984), The generation of vertical thermospheric winds and gravity waves at auroral latitudes—I. Observations of vertical winds, *Planet. Space Sci.*, *32*, 667–684, doi:10.1016/0032-0633(84)90092-8.

Rees, D., A. Aruliah, T. J. Fuller-Rowell, V. B. Wickwar, and R. J. Sica (1990), Winds in the upper mesosphere at mid-latitude: First results using an imaging Fabry-Perot interferometer, *Geophys. Res. Lett.*, *17*(9), 1259–1262, doi:10.1029/GL017i009p01259.

Reid, G. C. (1983), The influence of electric fields on radar measurements of winds in the upper mesosphere, *Radio Sci.*, *18*(18), 1028–1034, doi:10.1029/RS018i006p01028.

Rishbeth, H., and O. D. Garriott (1969), *Introduction to Ionosphere Physics*, Academic, New York.

Russell, J. P., W. E. Ward, R. P. Lowe, R. G. Roble, G. G. Shepherd, and B. Solheim (2005), Atomic oxygen profiles (80 to 115 km) derived from Wind Imaging Interferometer/Upper Atmospheric Research Satellite measurements of the hydroxyl and greenline airglow: Local time–latitude dependence, *J. Geophys. Res.*, *110*, D15305, doi:10.1029/2004JD005570.

Santos, P. T., C. G. M. Brum, C. A. Tepley, N. Aponte, S. A. González, and E. Robles (2011), Using incoherent scatter radar to investigate the neutral wind long-term trend over Arecibo, *J. Geophys. Res.*, *116*, A00H13, doi:10.1029/2011JA016514.

She, C. Y., S. Chen, B. P. Williams, Z. Hu, D. A. Krueger, and M. E. Hagan (2002), Tides in the mesopause region over Fort Collins, Colorado (41°N, 105°W) based on lidar temperature observations covering full diurnal cycles, *J. Geophys. Res.*, *107*(D18), 4350, doi:10.1029/2001JD001189.

Shepherd, G. G., et al. (1993), Longitudinal structure in atomic oxygen concentrations observed with WINDII on UARS, *Geophys. Res. Lett.*, *20*, 1303–1306, doi:10.1029/93GL01105.

Sivla, W. T., and Z. Mtumela (2012), Upper mesosphere and lower thermospheric wind response to a severe storm in the equatorial latitudes, *Adv. Appl. Sci. Res.*, *3*(6), 3831–3843.

Tsuda, T., and S. Kato (1988), Characteristics of semidiurnal tides observed by the Kyoto meteor radar and Saskatoon medium-frequency radar, *J. Geophys. Res.*, *93*, 7027–7036, doi:10.1029/JD093iD06p07027.

Tsuda, T., S. Kato, and R. A. Vincent (1988), Long period wind oscillations observed by Kyoto meteor radar and comparison of the quasi-2 day wave with Adelaide HF radar observations, *J. Atmos. Terr. Phys.*, *50*, 225–230, doi:10.1016/0021-9169(88)90071-2.

Won, Y. I., G. G. Sivjee, S. M. I. Azeem, and Q. Wu (2007), Tidal features in the wintertime mesospheric temperature and neutral winds recorded at Resolute Bay, Canada (74.68°N, 94.90°W), *J. Atmos. Terr. Phys.*, *69*, 459–470, doi:10.1016/j.jastp.2006.10.012.

Wu, Q., et al. (2004), A new Fabry-Perot interferometer for upper atmospheric research, *Proc. SPIE Int. Soc. Opt. Eng.*, *5660*, 218–227.

Wu, Q., R. D. Gablehouse, T. L. Killeen, and S. C. Solomon (2005), Multi-year high latitude mesospheric neutral wind observations using a Fabry-Perot interferometer, *Adv. Space Res.*, *35*, 1895–1899, doi:10.1016/j.asr.2005.05.112.

Xiong, J., W. Wan, B. Ning, L. Liu, and Y. Gao (2006), Planetary wave-type oscillations in the ionosphere and their relationship to mesospheric/lower thermospheric and geomagnetic disturbances at Wuhan (30.61°N, 114.51°E), *J. Atmos. Terr. Phys.*, *68*, 498–508, doi:10.1016/j.jastp.2005.03.018.

Xiong, J.-G., W. Wan, B. Ning, and L. Liu (2004), First results of the tidal structure in the MLT revealed by Wuhan meteor radar (30°40′N, 114°30′E), *J. Atmos. Terr. Phys.*, *66*, 675–682, doi:10.1016/j.jastp.2004.01.018.

Yamamoto, M., T. Tsuda, and S. Kato (1986), Gravity waves observed by Kyoto meteor radar in 1983-1985, *J. Atmos. Terr. Phys.*, *48*, 597–603, doi:10.1016/0021-9169(86)90094-2.

Yao, X., Y. Tao, Z. Biqiang, Y. You, L. Libo, N. Baiqi, and W. Weixing (2015), Climatological modeling of horizontal winds in the mesosphere and lower thermosphere over a mid-latitude station in China, *Adv. Space Res.*, *56*(2015), 1354–1365.

Yee, J. H., and V. J. Abreu (1987), Mesospheric 5577A green line and atmospheric motions-atmosphere explorer satellite observations, *Planet. Space Sci.*, *35*, 1389–1395, doi:10.1016/0032-0633(87)90051-1.

Yu, T., C. Huang, G. Zhao, T. Mao, Y. Wang, Z. Zeng, J. Wang, and C. Xia (2014), A preliminary study of thermosphere and mesosphere wind observed by Fabry-Perot over Kelan, China, *J. Geophys. Res. Space Physics*, *119*, 4981–4997, doi:10.1002/2013JA019492.

Yu, Y., W. Wan, B. Ning, L. Liu, Z. Wang, L. Hu, and Z. Ren (2013), Tidal wind mapping from observations of a meteor radar chain in December 2011, *J. Geophys. Res. Space Physics*, *118*, 2321–2332, doi:10.1029/2012JA017976.

Yuan, T., et al. (2006), Seasonal variation of diurnal perturbations in mesopause region temperature, zonal, and meridional winds above Fort Collins, Colorado (40.6°N, 105°W), *J. Geophys. Res.*, *111*, D06103, doi:10.1029/2004JD005486.

Yuan, W., J. Xu, R. Ma, Q. Wu, G. Jiang, H. Gao, X. Liu, and S. Z. Chen (2010), First observation of mesospheric and thermospheric winds by a Fabry-Perot interferometer in China, *Chin. Sci. Bull.*, *55*(35), 4046–4051, doi:10.1007/s11434-010-4192-2.

Yuan, W., X. Liu, J. Xu, Q. Zhou, G. Jiang, and R. Ma (2013), FPI observations of nighttime mesospheric and thermospheric winds in China and their comparisons with HWM07, *Ann. Geophys.*, *31*, 1365–1378, doi:10.5194/angeo-31-1365-2013.

Zhang, S. P., and G. G. Shepherd (1999), The influence of the diurnal tide on the O(S1S) and OH emission rates observed by WINDII on UARS, *Geophys. Res. Lett.*, *26*, 529–532, doi:10.1029/1999GL900033.

Zhang, S. P., J. E. Salah, N. Mitchell, W. Singer, Y. Murayama, R. R. Clark, A. van Eyken, and J. Thayer (2003), Responses of the mesospheric wind at high latitudes to the April 2002 space storm, *Geophys. Res. Lett.*, *30*(23), 2225, doi:10.1029/2003GL018521.

Zhao, G., L. Liu, W. Wan, B. Ning, and J. Xiong (2005a), Seasonal behavior of meteor radar winds over Wuhan, *Earth Planets Space*, *57*(1), 61–70, doi:10.1186/BF03351806.

Zhao, G., L. Liu, B. Ning, W. Wan, and J. Xiong (2005b), The turdiurnal tide in the mesosphere and lower thermosphere over Wuhan, *Earth Planets Space*, *57*(5), 393–398, doi:10.1186/BF03351823.

Zhou, X. (2015), Investigation on the differences between neutral wind speed and ionic velocity in the mid-latitude MLT on meteor radar, A Dissertation of University Students, Univ. of Scientist and Technology China.